



# Fatigue life assessment of wire arc additively manufactured ER100S-1 steel parts

Anna Ermakova<sup>1</sup> · Javad Razavi<sup>2</sup> · Rocco Crescenzo<sup>2</sup> · Filippo Berto<sup>2</sup> · Ali Mehmanparast<sup>1</sup>

Received: 20 September 2022 / Accepted: 7 January 2023  
© The Author(s) 2023

## Abstract

The aim of this work was to examine uniaxial, torsion, and multi-axial fatigue characteristics of ER100S-1 low carbon steel specimens fabricated with wire arc additive manufacturing (WAAM) technique, a subcategory of directed energy deposition (DED). Two distinct specimen orientations were tested—vertical and horizontal, extracted perpendicular and parallel to the WAAM deposited layers, respectively. Fracture surfaces of the tested specimens were analysed under scanning electron microscope (SEM) to observe fracture mechanisms corresponding to different specimen orientations, different fatigue loading conditions, and to interpret the fatigue results obtained from the tests. Finally, the obtained stress–life results were compared with the fatigue data available in the literature for a series of wrought and WAAM-built structural steel specimens. Moreover, the S–N curves obtained in this study were evaluated against the fatigue design curve recommended for offshore marine welded structures in DNV standard. Test results have shown advantageous characteristics of WAAM-built ER100S-1 specimens compared with behaviours of other structural steels and conservative prediction of its fatigue life by the design curve available in the DNV standard.

**Keywords** WAAM · Uniaxial · Torsion · Multiaxial fatigue · Steel

## List of symbols

$A$	Material-dependent constant
$B$	Material-dependent constant
$k$	Inverse slope in S–N curve
$N_f$	Number of cycles to failure
$R$	Load ratio
$T_\sigma$	Scatter index
$\lambda$	Biaxiality ratio
$\Delta\sigma$	Stress range
$\Delta\sigma_{50\%}$	Fatigue strength at $2 \times 10^6$ cycles
$\sigma_{\text{eff}}$	Effective stress
$\sigma_e$	Endurance limit
$\sigma_{\text{max}}$	Maximum stress
$\Phi$	Phase angle
AM	Additive manufacturing
CMT	Cold metal transfer

DED	Directed energy deposition
EDM	Electrical discharge machining
H	Horizontal
SB	Smooth round bars
SEM	Scanning electron microscope
V	Vertical
WAAM	Wire arc additive manufacturing

## 1 Introduction

Additive manufacturing (AM) is a comparatively new method of fabricating a product directly from a 3D computer model by adding material in layers, where each layer is a thin cross section from the corresponding 3D model [1]. This technique does not require any expensive moulds and production planning associated with conventional manufacturing procedures. Hence, it offers fabrication freedom, where the complexity of the final product form does not affect the manufacturing process. Since this process is based on adding material layer by layer rather than removing or subtracting it from a block of material, it is more sustainable and dramatically decreases the material waste. Even though all AM machines use a layer-based approach, the

✉ Ali Mehmanparast  
ali.mehmanparast@strath.ac.uk

<sup>1</sup> Department of Naval Architecture, Ocean and Marine Engineering, University of Strathclyde, Glasgow G1 1XQ, UK

<sup>2</sup> Norwegian University of Science and Technology (NTNU), Trondheim, Norway

final product characteristics will depend on the deposition process, layer thickness, the employed material, etc. Such differences will affect the dimensional accuracy, material properties and mechanical behaviour [2].

Directed energy deposition (DED) process, which is often referred to as ‘metal deposition’ technology, enables parts’ fabrication by melting material as it is being deposited. Wire arc additive manufacturing (WAAM) is a type of DED process that feeds and melts metal wire for deposition. It allows fabrication of functionally graded components by melting and mixing wires with different compositions. Fully dense parts are achievable by WAAM technique, with controllable microstructural features [3]. WAAM is the most effective for simple and bulky structures, without many thickness variations and with lower accuracy requirements, compared with powder-based techniques. WAAM provides the highest deposition rates amongst all AM methods (up to 5–8 kg/h depending on the employed material), whereas powder-based process can only offer up to 55 g/h [3, 4]. Hence, it reduces the manufacturing time by 40–60% as well as post-machining time by 20% compared with the conventional manufacturing methods [3]. Moreover, the WAAM process is designed to be pore-free, sacrificing the dimensional accuracy [5]. On the other hand, all the advantages of the new technique are balanced with the following common defect characteristics due to the welding nature of the process: locked-in residual stresses, poor surface finish, deformations, delamination, etc. [6]. Thus, some post-processing is usually required to address the above issues, such as machining, heat treatment and mechanical treatment on the WAAM wall surfaces. Also, the repetitive cycles of heating and cooling during the manufacturing process can lead to microstructural variations and anisotropic behaviour of the WAAM part [7–10].

The majority of failures in engineering structures and machinery are caused by fatigue [11]. Such failures usually happen with little warning, thus may bring catastrophic consequences. Therefore, fatigue of materials is an essential study for any new material and manufacturing technique in modern industries. This includes a broad variety of complex mechanical testing, investigating different stages of fatigue damage, to control nucleated cracks and prevent the final fatigue failure [12]. Having said that, fatigue assessment becomes crucial for AM built components that consist of welding defects and tensile residual stresses—two major factors contributing to the fatigue failures [13]. Some industries, such as aerospace and automotive, have already introduced and are widely implementing AM processes. Thus, the majority of reported data on fatigue performance of AM (and WAAM in particular) are for titanium [6, 14–17] and stainless steel [18, 19]. However, only limited information is available on structural steels, which is required

for promoting AM techniques in other industrial sectors, including civil engineering and renewable energy and offshore structures.

In previous work carried out by Dirisu et al. [20], fatigue experiments were conducted to investigate the failure behaviour of ER70S-6 WAAM-built flat dog bone specimens extracted in horizontal orientation (i.e. along deposited layers). Three different specimen types were examined: as-built, as-built with rolling surface treatment applied, and machined. All specimens were subjected to pure uniaxial loading conditions with the load ratio of  $R=0.1$ . The experimental results revealed the higher fatigue strength of the machined specimens compared with other two types of as-built specimens with poor surface finishes, confirming that smooth surface prolongates the fatigue life. However, rolling surface treatment was also found to be an effective method for fatigue life enhancement of the specimens when compared with just as-built specimens. Another study was carried out by Bartsch et al. [13] on G3Si1 WAAM as-built dog bone specimens. Two different specimen lengths were examined under uniaxial fatigue loading with the load ratio of  $R=0.1$ . Similarly, it was discovered that the surface waviness acts as the stress riser and is the main influencing factor affecting the life span of the tested specimens.

It can be seen from the above literature review that only a few data sets on fatigue performance were generated for WAAM-built structural steel specimens, covering only uniaxial fatigue loading condition. To fill the gap in the knowledge, the present study was conducted, investigating the fatigue behaviour of ER100S-1 WAAM-built specimens under different cyclic loading conditions. The current study includes a broad fatigue analysis under uniaxial, torsion and multi-axial loading conditions, generating stress–life plots. Moreover, the sensitivity of the fatigue life to the specimen extraction orientation was examined for each of the cyclic loading conditions considered in this study. Furthermore, the obtained data from this study were compared with the existing fatigue data for conventionally built structural steel specimens and with the recommended design curve for welded structures in international standards. Finally, the fracture surfaces of the broken specimens were carefully observed under the microscope to better understand the failure mechanisms inherent in specimens with different orientations tested under different fatigue loading conditions.

## 2 Specimen preparation process

The fatigue tests were conducted on the specimens that were produced by means of WAAM process. Four WAAM walls were manufactured using Böhler Welding ER100S-1 [21] low carbon steel wire, with the chemical composition presented in Table 1. The Cold Metal Transfer (CMT)-based

**Table 1** Chemical composition of ER100S-1 material (wt.-%) [21]

	C	Mn	Cr	Si	Ni	Mo
ER100S-1	0.08	1.70	0.20	0.60	1.50	0.50

**Table 2** CMT-WAAM fabrication parameters

Shielding gas	Ar + 20% CO <sub>2</sub>
Gas flow rate	15 L/min
Wire diameter	1.2 mm
Robot travelling speed	7.33 mm/s
Wire feed speed	7.5 m/min
Dwell time	120 s

WAAM system was employed with the fabrication parameters highlighted in Table 2, which were maintained during the manufacturing process, to minimise the microstructural variabilities throughout deposited layers and amongst all of the built walls. The automatic WAAM-CMT system set-up is displayed in Fig. 1a, which consists of the CMT power source with a mounted wire spool, a pre-programmed robotic arm that supplies both wire and shielding gas through the torch simultaneously, a workbench on which the base plate was clamped to, and an exhaust fan positioned above the manufacturing area to remove the excess of the heat and fumes generated during the process. The base plate was cut from a plate of the wrought EN10025 rolled structural steel, with dimensions of  $420 \times 200 \times 12 \text{ mm}^3$ . It was fixed onto the working table with eight clamps, to minimise bending and distortion of the plate and hence the WAAM wall due to high fabrication temperatures. Prior to releasing the clamps and upon completion of the wall deposition, the time was allowed for the wall to cool down to the ambient temperature. Additive layers were deposited in the middle of the base plate, in oscillation manner [22] to attain the desired

thickness of 24 mm (Y-axis in Fig. 1a), the wall length of approximately 355 mm (X-axis) and height of 140 mm (Z-axis).

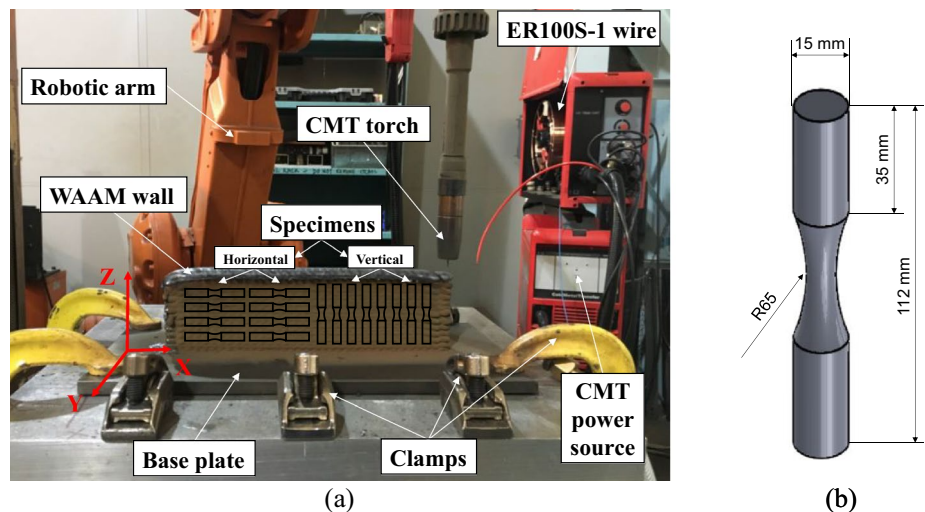
Sixty smooth round bar (SB) specimens were extracted from the manufactured ER100S-1 WAAM walls using Electrical Discharged Machining (EDM) process. The round bar specimens were designed in accordance with the ASTM E466 standard [23] with the dimensions presented in Fig. 1b. A schematic of the extraction plan for one wall is shown in Fig. 1a, where it can be seen that the specimens were cut in two different orientations: vertical (V)—along Z-axis and perpendicular to the deposited AM layers, and horizontal (H)—along X-axis and deposited layers, to conduct the sensitivity analysis of the fatigue response to the built orientation.

### 3 Experimental and analysis procedures

#### 3.1 Fatigue tests

Three types of fatigue tests were conducted in this study: uniaxial, torsion, and multi-axial. All tests were performed using an MTS landmark servo-hydraulic machine with the maximum load capacity of 100 kN, under load control mode. The test parameters in all experiments were as follows: frequency of 20 Hz and the load ratio of  $R = 0.01$ . For multi-axial fatigue tests, in-phase loading was applied,  $\Phi = 0^\circ$ , with the biaxiality ratio of  $\lambda = 1$ . The Wöhler curves were obtained separately for vertical and horizontal specimens, testing on average 10 specimens for each loading

**Fig. 1** **a** WAAM-CMT system set-up with schematic extraction plan for specimens from a built wall, and **b** cylindrical specimen dimensions



type (uniaxial, torsion and multi-axial), recording the maximum stress  $\sigma_{\max}$  and number of cycles at failure  $N_f$  for each test case. In this study, the specimens that endured  $2 \times 10^6$  cycles, were considered as run-outs. The collected test data were then analysed using the Basquin relationship, correlating the number of cycles to failure  $N_f$  with the cyclic stress range  $\Delta\sigma$  using a power-law expression of  $N_f = A(\Delta\sigma)^B$ . In this equation,  $A$  and  $B$  are the material-dependent coefficients that can be obtained from a line of best fit made to the experimental data.

The fatigue data were subsequently analysed by plotting 10% (upper bound), 50% (mean curve) and 90% (lower bound) probability of survival bands based on the procedure defined in ASTM E739-10 [24] and BS ISO 12107:2003 [25] standards. The inverse slope  $k = 1/B$ , scatter index  $T_\sigma$  and the fatigue strength were identified for each stress–fatigue life diagram. In this analysis,  $T_\sigma$  was computed as a ratio between the stress levels corresponding to the 10% and 90% survival probabilities.

### 3.2 Fractography

Failure mechanisms were examined by conducting the microscopy analysis on specimens with different orientations subjected to different fatigue load conditions (uniaxial, torsion and multi-axial). The fractography examination was performed using the FEI Quanta 650 FEG scanning electron microscope (SEM). For direct comparison of the fracture surfaces after fatigue testing in specimens with different orientations, specimens subjected to the similar load levels were selected for post-mortem analysis. The recorded observations from the fractography analysis were then correlated with the experimental fatigue data for an accurate interpretation of fatigue life assessment of WAAM-built ER100S-1 specimens with different orientations tested under different fatigue load types.

## 4 Tests results and discussion

### 4.1 Fatigue test results

The obtained fatigue data from ER100S-1 WAAM specimens for different loading types and specimen orientations were analysed according to the procedure described in Sect. 3.1 by plotting the maximum stress against number of cycles to failure in log–log axes presented in Fig. 2, and by determining the fatigue properties: fatigue strength at  $2 \times 10^6$  cycles,  $\Delta\sigma_{50\%}$ , the scatter index  $T_\sigma$ , and the inverse slope factor  $k$ , which were are summarised in Table 3. The fatigue data from the uniaxial tests are shown in Fig. 2a for vertical specimens, Fig. 2b for horizontal and Fig. 2c direct comparison of two trends. The run-out data for both specimen

orientations suggest that the alloy exhibits a plateau at the low stress values in the stress–life plot, known as the endurance limit,  $\sigma_e$ . Based on the obtained experimental data, the endurance limit for the vertical specimens is found to be between 600 and 575 MPa, and for the horizontal specimens between 575 and 550 MPa. Hence, both vertical and horizontal specimen orientations have similar endurance limit within 4.1%, with slightly higher value for the vertically oriented specimens. Based on the previous study by Ermakova et al. [26], different orientations of WAAM-built ER100S-1 specimens have very similar yield and ultimate tensile strength values (under 1% difference); hence, the obtained trend is confirmed and reflected in values of uniaxial fatigue endurance limits in this study. It is also worth noting that the obtained endurance limits for the vertical and horizontal specimens are above the yield strength of the material, which is 536 MPa and 538 MPa, respectively. Comparison of the maximum stress against number of cycles to failure curves for different specimens' orientations in Fig. 2c shows that the slope for the vertical specimens curve is steeper than for horizontal; this is also indicated by the inverse slope factor that is 1.2 times higher for the horizontally oriented specimens, presented in Table 3. Also seen in the table, the scatter index for the obtained data sets from uniaxial test is comparable for the specimens with different orientations and only differs by 2.3%. Finally, the plotted data display that at lower cycles, both specimen orientations exhibit similar behaviour under uniaxial fatigue loading condition; however, the trend changes with the increase in the number of cycles.

Assessment of the torsion fatigue results demonstrated in Fig. 2d–f reveals that the trends are independent of the specimen orientation and fall on top of each other, with identical torsion fatigue strength of 457 MPa. The slope of the two curves only differs by 1.3%, with the data points falling slightly apart at higher stress values and converging towards the lower stress values. However, the scatter index (Table 3) is 11.4% higher for the horizontal specimens than for vertical. Comparable torsion fatigue behaviour for two specimen orientations can also be attributed to the similar tensile characteristics of the material, including its ductility [26].

The multi-axial fatigue results for WAAM-built ER100S-1 specimens are shown in Fig. 2g–i. From the figures, it can be seen that the 50% survival probability lines of the data sets for vertical and horizontal specimens are almost parallel to each other, with the vertical curve falling above the horizontal. The inverse slope factors for two trends differ by 5.7%, and similar to the pattern observed in torsion fatigue results, two curves are converging towards low stress (high cycle) fatigue results. The multi-axial fatigue strength for vertical specimens is 356 MPa and is 3.9% higher than for horizontal specimens, with fatigue strength of 342 MPa. The scatter for the obtained data sets is 3.8% higher for the

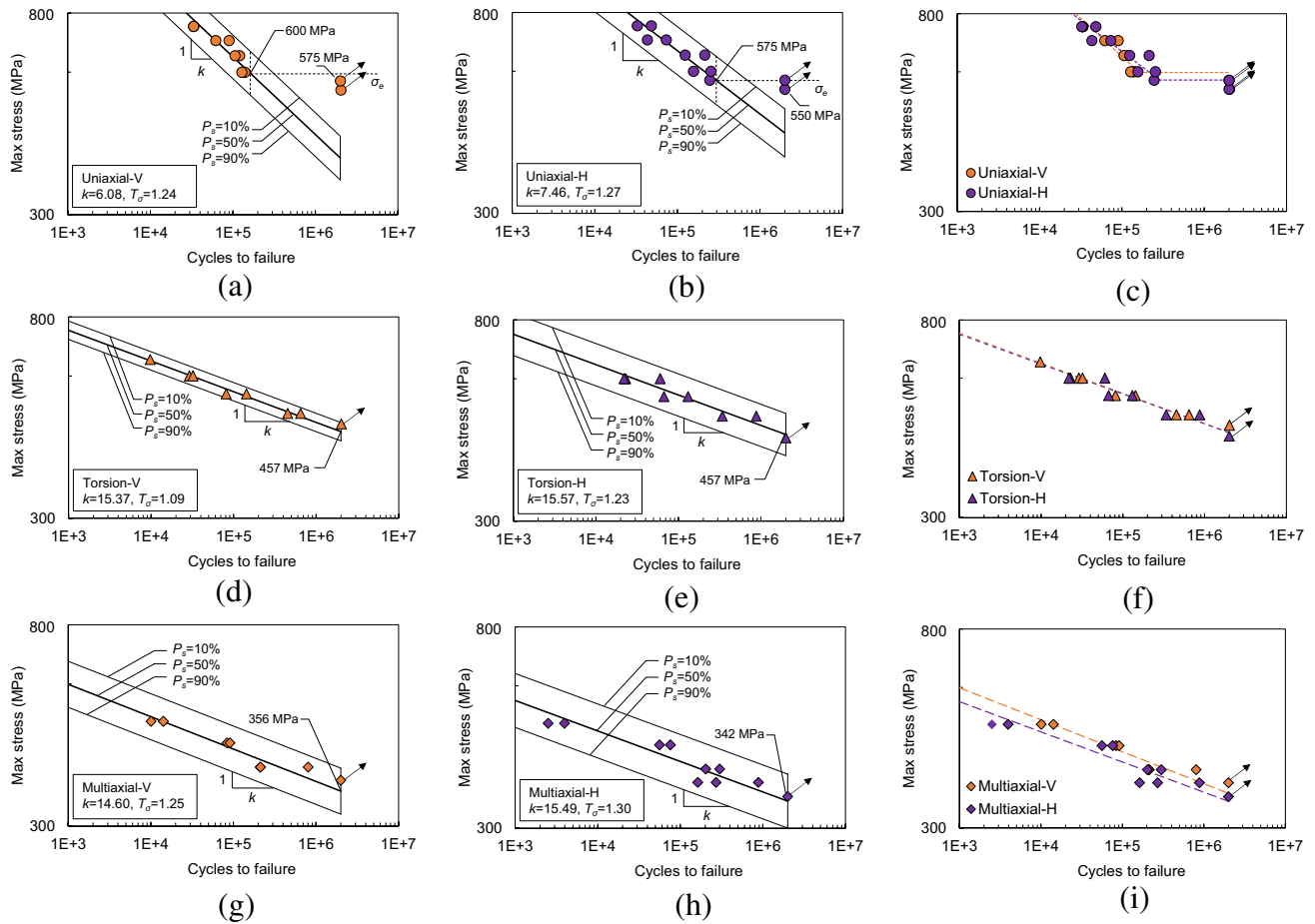


**Fig. 2** Fatigue data for ER100S-1 specimens **a–c** axial, **d–f** torsion, **g–i** multi-axial tests

**Table 3** Fatigue properties of tested ER100S-1 specimens

Test	Orientation	$\Delta\sigma_{50\%}$ [MPa]	$T_\sigma$	$k$
Uniaxial	V	600	1.24	6.08
	H	575	1.27	7.46
Torsion	V	457	1.09	15.37
	H	457	1.23	15.57
Multiaxial	V	356	1.25	14.60
	H	342	1.30	15.49

horizontal specimens than for vertical as seen by the scatter index summarised in Table 3.

The obtained data sets for all fatigue tests for vertical and horizontal specimens were then compared with each other in Fig. 3. As expected, it is seen from this figure that the overall fatigue strength of material is decreasing from uniaxial fatigue to torsion and, similarly, from torsion to multi-axial fatigue test results. Considering the values summarised in Table 3, the average fatigue strength of ER100S-1 WAAM components (i.e. the mean value between fatigue

strength of vertical and horizontal specimens) drops by 22.2% for torsion tests compared with the average endurance limit obtained in uniaxial tests, and further by 23.6% for results obtained under multi-axial applied stress. This leads to a conclusion that the fatigue strength of WAAM-built ER100S-1 specimens strongly depends on the type of the applied fatigue loading condition, as expected. Another observation that can be made from Fig. 3 is that the slopes for the data from torsion and multi-axial fatigue tests are almost parallel to each other, whilst for uniaxial fatigue, it is approximately two times steeper. Thus, the reduction of the applied stress values towards the high cycle fatigue region is more pronounced in tests under pure uniaxial loading condition. Furthermore, analysis of the data obtained from different specimen orientations shows negligible variability of the results, with the maximum range within 4.1% for pure uniaxial tests, so the material can be considered to be insensitive to the built specimen orientation in fatigue performance. Nevertheless, the trends presented in Fig. 3 reveal that even with minor difference, the vertical specimens' mean curves are above horizontal in cases of torsion and



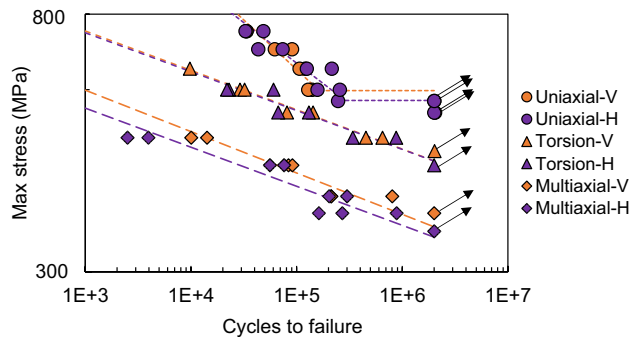


**Fig. 3** Comparison of all fatigue experimental data for ER100S-1 WAAM specimens

multi-axial fatigue loading conditions. On the other hand, uniaxial test results show that the horizontal specimen mean curve is above the vertical within a range between 48,700 and 255,300 cycles, otherwise the vertical specimens exhibit higher fatigue life. It was reported in previous studies that in certain test scenarios (fracture toughness [26] and fatigue crack growth [27]), ER100S-1 WAAM-built specimens are insensitive to the built orientation, but their performance is highly dependent on the extraction location instead (top or bottom of the WAAM wall). Thus, further study needs to be carried out in the future work to investigate the sensitivity of the fatigue performance of ER100S-1 WAAM specimens to the specimen extraction location.

#### 4.2 Comparison with the literature data on steel specimens and standard design curves

The performance of the 50% uniaxial fatigue failure bands (i.e. mean curves) obtained from this study for WAAM ER100S-1 was further analysed for application in offshore structures, by comparing the data with the S–N fatigue C1 design curve, recommended by the DNV RP-C203 standard [28] for structures with the continuous welds and ground flush surface finish. The results from this comparison have been presented in log–log axes in Fig. 4. It is seen in this figure that both vertical and horizontal specimen orientation trends fall above the recommended DNV standard C1 design curve. Moreover, the tested material is exhibiting the fatigue endurance limit at much higher stress range values and lower number of cycles than suggested in the standard. The slopes of the experimental curves are lower compared with the DNV C1 curve. To conclude, the stress–life plot proposed by the standard provides a conservative estimation of the ER100S-1 WAAM specimens tested under pure uniaxial loading conditions. Hence, this material and manufacturing technique can be considered for offshore structures production and repair.

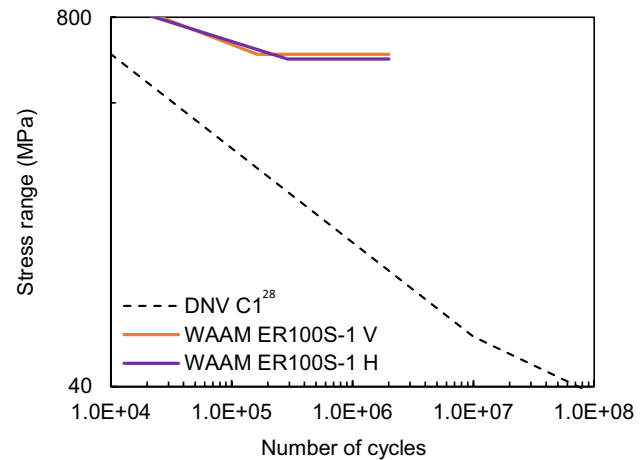


**Fig. 4** Comparison of uniaxial fatigue data for WAAM ER100S-1 specimens with DNV C1 recommended design curve

Extensive comparison with the data on uniaxial, torsion and multi-axial fatigue performance of other structural steels available in the literature was also conducted. Knowing that the fatigue behaviour of the material strongly depends on the testing parameters, such as load ratio  $R$ , and specimens' design [29, 30], all the collected data with various load ratios were normalised into a single fatigue plot using the effective stress  $\sigma_{\text{eff}}$  model, defined in Equation. This concept was invented for the direct comparison of fatigue data from different studies [31]; however, it does not consider the effects of different loading frequencies. Therefore, some limited effects from different fatigue frequencies and specimen designs are expected in the following comparison.

$$\sigma_{\text{eff}} = \sigma_{\text{max}} \left( \frac{1-R}{2} \right)^{0.28} \quad (1)$$

The mean uniaxial fatigue plots for ER100S-1 WAAM specimens were compared with the limited data sets on S355 wrought steel specimens available in the literature. S355 is a structural steel which is typically used in fabrication of offshore structures in renewable energy sector [32, 33]. Hence, such comparison will provide a better understanding of suitability of WAAM-built components for marine renewable energy applications. The uniaxial fatigue data which were used for comparison include: the data obtained from large dog bone S355 specimens tested at  $R=0.1$  tested by Anandavijayan et al. [34], the data from smaller dog bone S355 specimens examined at  $R=-1$  by Corigliano et al. [35], the data from round bar S355 specimens assessed at  $R=0.01$  by Dantas et al. [36] and at  $R=-1$  by Aeran et al. [37], and finally the data from fillet welded cruciform S355 specimens tested at  $R=0$  by Berto et al. [38]. The S–N curve, generated for

wrought cylindrical C40 carbon steel specimens at  $R = -1$  by Atzori et al. [39] was also included into the comparison with the literature data. Along with limited results from studies on WAAM-built specimens, the ER70S-6 flat dog bone specimens tested at  $R = 0.1$  by Dirisu et al. [20] and G3Si1 as-built (with rough surface) flat dog bone specimens with two different specimens designs examined at  $R = 0.1$  by Bartsch et al. [13] were also included in the comparison with the literature data. The above data sets were normalised to effective stress (see Equation) and presented in log–log axes in Fig. 5a. It can be seen in this figure that the fatigue results obtained from ER100S-1 WAAM specimens fall above the collected data from the

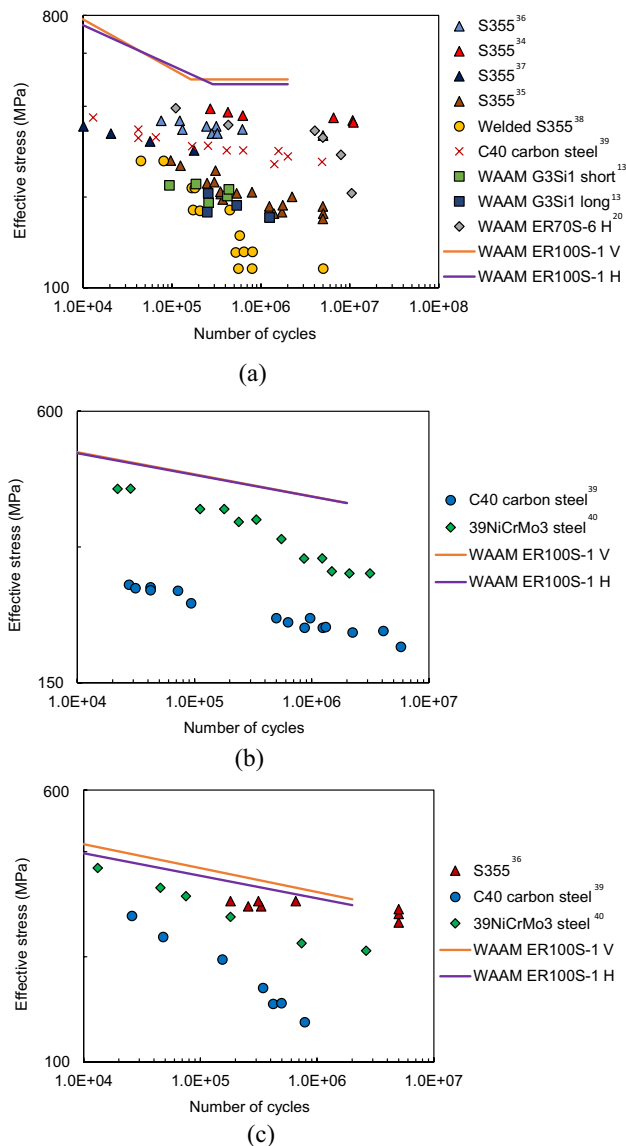


**Fig. 5** Comparison of fatigue data for WAAM ER100S-1 with data in the literature for **a** uniaxial, **b** torsion, and **c** multi-axial fatigue tests on steel

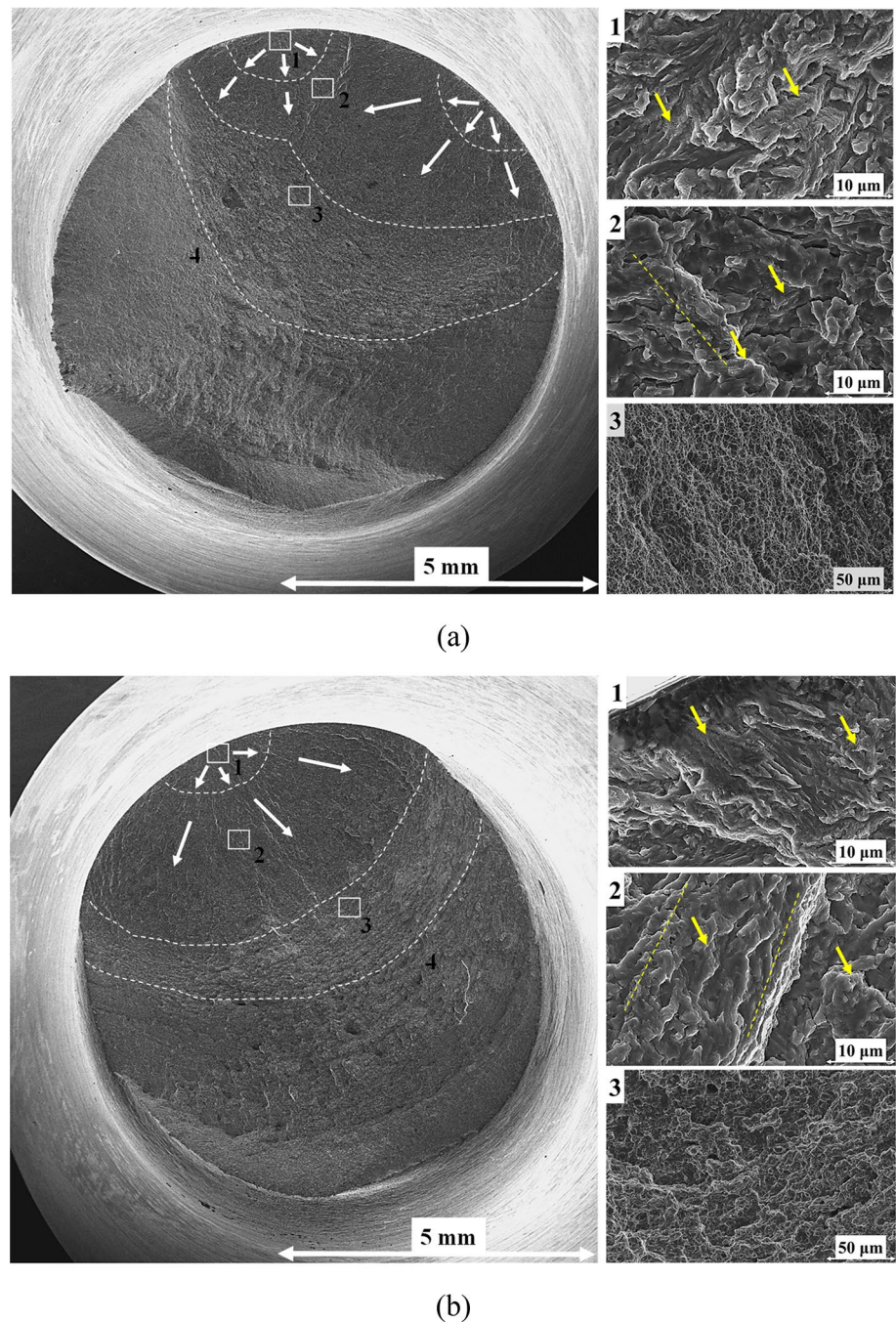
literature on wrought S355, C40 and WAAM ER70S-6 and G3Si1 steels. The slopes of the curves for ER100S-1 uniaxial fatigue are similar to some stress–life plots for S355 and WAAM G3Si1 specimens. Moreover, due to the fatigue endurance limit of ER100S-1 specimens, both data sets for vertical and horizontal orientations are not crossing the rest of the S–N curves even at higher number of cycles. However, it must be noted here that yield and ultimate tensile strengths of ER100S-1 material are relatively higher than any of the presented materials. Thus, it is expected that uniaxial fatigue performance is also found to be superior.

Only a few data sets on torsion and multi-axial fatigue were collected and presented in this comparative study due to limited availability of such data on structural steels in the literature. The comparison of the effective stress versus number of cycles to failure in log–log axes for the results obtained from this study with the literature data is presented in Fig. 5b, c for torsion and multi-axial fatigue loading conditions, respectively. A previous study reported that the performance of round bar C40 carbon steel specimens was tested with loading ratio of  $R = -1$  under torsion and with  $R = 0$  under multi-axial loading conditions by Atzori et al. [39]. Another study provided some data on round bar 39NiCrMo3 steel specimens assessed at  $R = -1$  by Berto et al. [40]. Additionally, a curve for multiaxial fatigue on round bar wrought S355 specimens examined at  $R = 0.01$  by Dantas et al. [36] was added for comparison. The bi-axiality ratio for all presented multiaxial fatigue data in this analysis was  $\lambda = 1$ , with in-phase loading angle of  $\Phi = 0^\circ$ . It can be seen in Fig. 5b, c that similar to the case of uniaxial fatigue, the results for torsion and multiaxial life assessment fall above the data from the literature. The trends for C40 and 39NiCrMo3 steels are below and parallel to the trends obtained from this study for ER100S-1 WAAM specimens under torsion fatigue condition. Moreover, the multi-axial behaviour of ER100S-1 has been found similar to the data on S355 wrought steel.

## 5 Fractography analysis

The microstructural analysis of the tested specimens conducted using SEM revealed almost defect-free surfaces of WAAM-built ER100S-1 specimens, with rare minor defects under  $20\ \mu\text{m}$ . The fractography assessment of the tested specimens was conducted to examine the fracture surfaces and establish any differences in failure mechanisms for specimens with different orientations tested under different fatigue loading conditions (i.e. uniaxial, torsion, and multi-axial). Figure 6 displays two fracture surfaces of (a) vertical and (b) horizontal specimens tested under pure uniaxial fatigue with maximum

**Fig. 6** Fracture surfaces of ER100S-1 WAAM **a** vertical and **b** horizontal specimens tested under uniaxial fatigue loading condition



stress of 650 MPa. Four clear crack growth stages can be observed on both fracture surfaces: 1—crack nucleation point, 2—crack propagation, 3—ductile failure due to unstable fatigue crack growth, and 4—ductile failure caused by fast fracture. Moreover, the fracture surface of the vertical specimen in Fig. 6a exhibited two nucleation points, in which two cracks initiated simultaneously on parallel planes and then consequently converged into one crack in propagation region depicted as 2. White arrows in the figures indicate the direction of the crack growth in both specimens. The crack initiation in both cases started

from the surface irregularities. The fatigue life of horizontal specimen was twice longer than for vertical, which can be caused by the two initial cracks nucleated in the vertical specimen contributing to the early final failure of the specimen. Examination of the crack growth regions at higher magnification shows that the transition from one grain to other leads to the change of the fracture plane caused by different orientation of individual grains. Moreover, the fatigue striations can be seen in crack initiation and propagation regions for both specimens (shown with yellow arrows), which are parallel to the crack propagation

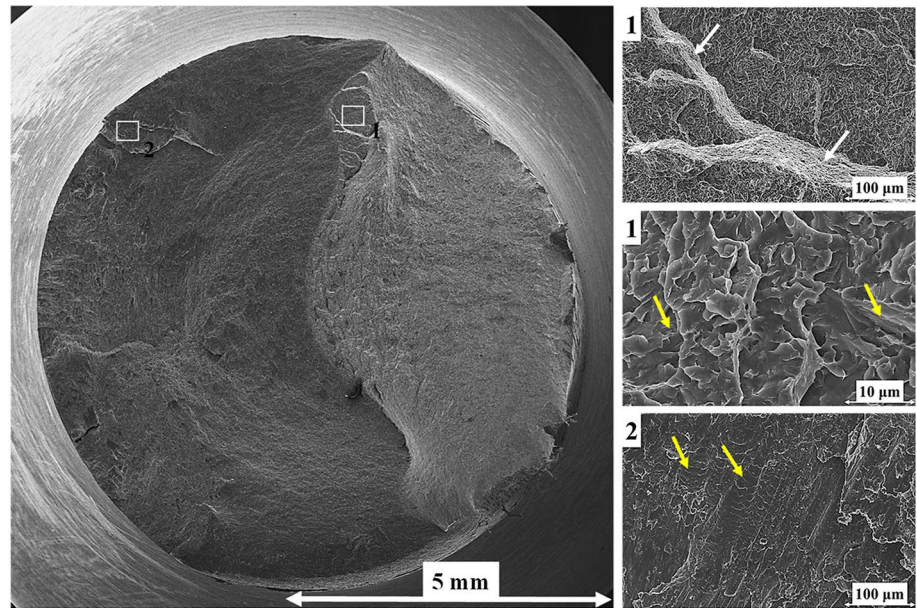


direction. Furthermore, in crack growth propagation region 2 in both specimens, elongated fracture features can be observed (highlighted with dashed yellow lines), which indicate the crack propagation direction. The fracture surfaces in regions 1 for both vertical and horizontal specimens present shallower ductile features, whilst in regions 2, the dimples become bigger and deeper, and secondary cracks are visible. To conclude, no major difference in failure mechanisms was observed for specimens with different extraction orientations. Moreover, similar

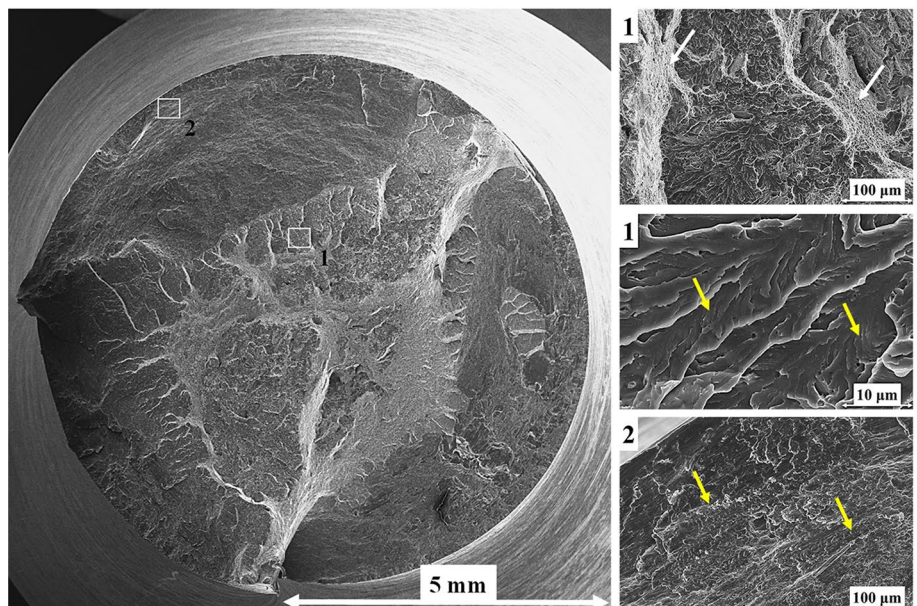
fracture features revealed during the analysis, which are in good agreement with similar uniaxial fatigue and mechanical performance of the vertical and horizontal ER100S-1 WAAM specimens.

Two fracture surfaces for vertical and horizontal ER100S-1 WAAM specimens examined under pure torsion fatigue with maximum stress of 550 MPa are presented in Fig. 7a, b respectively. It is seen from the figures that in both cases, the outer diameter of the fracture surface is not entirely flat, consisting of the series of inclined surfaces,

**Fig. 7** Fracture surfaces of ER100S-1 WAAM **a** vertical and **b** horizontal specimens tested under torsion fatigue loading condition



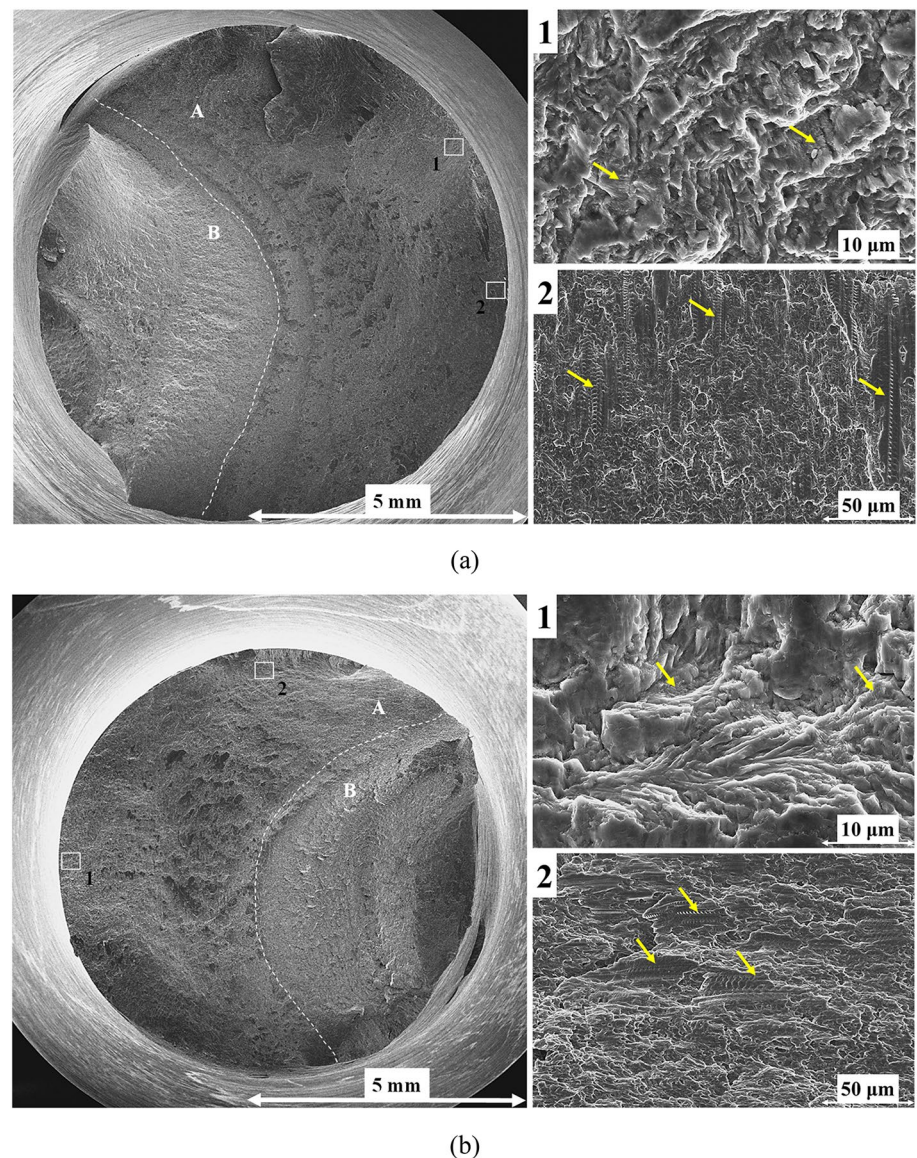
(a)



(b)



**Fig. 8** Fracture surfaces of ER100S-1 WAAM **a** vertical and **b** horizontal specimens tested under multi-axial fatigue loading condition



so called ‘factory roof’ morphology [40, 41], initiated due to presence of torsion fatigue (out-of-plane shear in mode III) and transforming to pronounced inclined features under mode I. Larger area of fracture surface of the vertical specimen shows the presence of abrasion, caused by mode III loading condition, demolishing the fracture features by rubbing two fracture surfaces against each other. For horizontal specimen, the damaged area is much smaller (approximately half of the full fracture surface) and located in the centre of the fracture surface. This was also indicated in number of cycles to failure, which was 1.2 times lower for the horizontal specimen than for vertical. The area with remaining fatigue fracture features is a result of the final failure of the specimen under mode I loading condition, forming a cascade of fatigue fracture planes, also shown in the regions 1 in Fig. 7. Closer examination of the area reveals the ductile

fatigue facets (yellow arrows in region 1), which appear as river patterns under lower magnification (white arrows in region 1). Another interesting fatigue feature was observed near the edge of the fracture surface in both specimens—colonies of flat ‘fish-bone’ features, representing smaller and less ductile facets formed due to initial short crack growth, perpendicular to the fracture edge of the specimens (yellow arrows in region 2).

Lastly, two fracture surfaces of the specimens previously subjected to multi-axial fatigue loading conditions under maximum stress of 450 MPa were examined and shown in Fig. 8a for vertical and (b) for horizontal broken specimens. Similar to the specimens tested under torsion, the edges of the fracture surfaces in Fig. 8 are not flat and present some ‘factory roof’ morphology with inclined surfaces formed in combination of applied mode I and III fracture

loading conditions. Approximately 60% of the fracture surfaces (region A) indicate evidence of abrasion and wear, occurred under mode III out-of-plane shear mechanisms. Two main fatigue features were found in this region and are highlighted with yellow arrows: 1—fatigue striations, and 2—‘fish-bone’ colonies, representing large striations near the fracture edges of the specimens. The latter feature appears in specimens tested under pure tension and multi-axial fatigue, hence is the evidence of the torsion fracture mechanisms resulted under mode III. The remaining fracture surface area depicted as B is due to the final specimen failure in fast fracture with corresponding cup and cone shapes.

## 6 Conclusions

A series of fatigue tests were performed on WAAM-built ER100S-1 specimens that were extracted along two different orientations: vertical and horizontal. Uniaxial, torsion, and multi-axial fatigue behaviour of the specimens was examined by developing the stress–life plots. The following observations and conclusions were made from this study:

- Uniaxial, torsion, and multi-axial fatigue properties of WAAM ER100S-1 specimens are not dependant on the specimen orientation.
- The fatigue strength of the material obtained from torsion tests drops by 22.2% compared with uniaxial test results; and further by 23.6% under multi-axial fatigue loading.
- Trends for uniaxial, torsion and multi-axial fatigue show advantageous performance of WAAM ER100S-1 specimens compared with other structural steels, including S355 steel that is commonly used in offshore structures.
- The S–N fatigue behaviour of ER100S-1 WAAM-built material can be conservatively predicted by DNV C1 standard design curve for structures with continuous welds and ground flush surface finish.
- The examined WAAM-built specimens were found to be almost defect-free, with minor defects of smaller than 20  $\mu\text{m}$ . The study of fracture surfaces of six specimens revealed common fatigue features for each of the fatigue load types, with no significant variations between vertical and horizontal specimens.

**Acknowledgements** This work was supported by grant EP/L016303/1 for Cranfield, Oxford and Strathclyde Universities’ Centre for Doctoral Training in Renewable Energy Marine Structures—REMS CDT (<http://www.remscdt.ac.uk/>) from the UK Engineering and Physical Sciences Research Council (EPSRC).

**Data availability** Data will be made available on request.

**Open Access** This article is licensed under a Creative Commons Attribution 4.0 International License, which permits use, sharing, adaptation, distribution and reproduction in any medium or format, as long as you give appropriate credit to the original author(s) and the source, provide a link to the Creative Commons licence, and indicate if changes were made. The images or other third party material in this article are included in the article's Creative Commons licence, unless indicated otherwise in a credit line to the material. If material is not included in the article's Creative Commons licence and your intended use is not permitted by statutory regulation or exceeds the permitted use, you will need to obtain permission directly from the copyright holder. To view a copy of this licence, visit <http://creativecommons.org/licenses/by/4.0/>.

## References

1. ISO/ASTM International (2015) ISO/ASTM 52900: additive manufacturing—general principles and Terminology. Int Stand 5:1–26
2. Gibson I, Rosen D, Stucker B, Khorasani M (2020) Additive Manufacturing Technologies. Yosetsu Gakkai Shi/Journal of the Japan Welding Society, vol 89. Springer
3. Wu B, Pan Z, Ding D, Cuiuri D, Li H, Xu J, Norrish J (2018) A review of the wire arc additive manufacturing of metals: properties, defects and quality improvement. J Manuf Process 35:127–139
4. Seow CE, Zhang J, Coules HE, Wu G, Jones C, Ding J, Williams S (2020) Effect of crack-like defects on the fracture behaviour of Wire + Arc Additively Manufactured nickel-base Alloy 718. Addit Manuf 36:101578
5. Rodrigues TA, Duarte V, Miranda RM, Santos TG, Oliveira JP (2019) Current status and perspectives on wire and arc additive manufacturing (WAAM). Materials 12:1121
6. Fotovvati B, Namdari N, Dehghanghadikolaie A (2019) Fatigue performance of selective laser melted Ti6Al4V components: State of the art. Mater Res Express 6:012002. <https://doi.org/10.1088/2053-1591/aae10e>
7. Baufeld B, Brandl E, Van Der Biest O (2011) Wire based additive layer manufacturing: Comparison of microstructure and mechanical properties of Ti–6Al–4V components fabricated by laser-beam deposition and shaped metal deposition. J Mater Process Technol 211:1146–1158
8. Ding J, Colegrove P, Mehnen J, Ganguly S, Almeida PMS, Wang F, Williams S (2011) Thermo-mechanical analysis of Wire and Arc Additive Layer Manufacturing process on large multi-layer parts. Comput Mater Sci 50:3315–3322
9. Domashenkov A, Plotnikova A, Movchan I, Bertrand P, Peillon N, Desplanques B, Saunier S, Desrayaud C (2017) Microstructure and physical properties of a Ni/Fe-based superalloy processed by Selective Laser Melting. Addit Manuf 15:66–77
10. Todai M, Nakano T, Liu T, Yasuda HY, Hagiwara K, Cho K, Ueda M, Takeyama M (2017) Effect of building direction on the microstructure and tensile properties of Ti-48Al-2Cr-2Nb alloy additively manufactured by electron beam melting. Addit Manuf 13:61–70
11. ASM (2008) ASM International Fatigue. Elem Metall Eng Alloy, pp 243–265
12. Suresh S (1998) Fatigue of materials. Fatigue Mater. <https://doi.org/10.1017/CBO9780511806575>
13. Bartsch H, Kühne R, Citarelli S, Schaffrath S, Feldmann M (2021) Fatigue analysis of wire arc additive manufactured (3D printed) components with unmilled surface. Structures 31:576–589
14. Biswal R, Zhang X, Shamir M, Al Mamun A, Awd M, Walther F, Khadar Syed A (2019) Interrupted fatigue testing with periodic

- tomography to monitor porosity defects in wire + arc additive manufactured Ti-6Al-4V. *Addit Manuf* 28:517–527
15. Pegues J, Roach M, Scott Williamson R, Shamsaei N (2018) Surface roughness effects on the fatigue strength of additively manufactured Ti-6Al-4V. *Int J Fatigue* 116:543–552
  16. Syed AK, Zhang X, Caballero A, Shamir M, Williams S (2021) Influence of deposition strategies on tensile and fatigue properties in a wire + arc additive manufactured Ti-6Al-4V. *Int J Fatigue* 149:106268
  17. Shamir M, Syed AK, Janik V, Biswal R, Zhang X (2020) The role of microstructure and local crystallographic orientation near porosity defects on the high cycle fatigue life of an additive manufactured Ti-6Al-4V. *Mater Charact* 169:110576
  18. Zulić S, Rostohar D, Kaufman J, Pathak S, Kopeček J, Böhm M, Brajer J, Mocek T (2022) Fatigue life enhancement of additive manufactured 316L stainless steel by LSP using a DPSS laser system. *Surf Eng*. <https://doi.org/10.1080/02670844.2022.2060463>
  19. Shrestha R, Simsiriwong J, Shamsaei N (2021) Fatigue behavior of additive manufactured 316L stainless steel under axial versus rotating-bending loading: Synergistic effects of stress gradient, surface roughness, and volumetric defects. *Int J Fatigue* 144:106063
  20. Dirisu P, Supriyo G, Martina F, Xu X, Williams S (2020) Wire plus arc additive manufactured functional steel surfaces enhanced by rolling. *Int J Fatigue* 130:105237
  21. ER100S-G Data Sheet-Bohler Welding (2014)
  22. Ermakova A, Mehmanparast A, Ganguly S (2019) A review of present status and challenges of using additive manufacturing technology for offshore wind applications. *Proc Struct Integr* 17:29–36
  23. Standard Practice for Conducting Force Controlled Constant Amplitude Axial Fatigue Tests of Metallic Materials. <https://www.astm.org/e0466-21.html>. Accessed 5 July 2022
  24. Testing F (2009) Standard practice for statistical analysis of linear or linearized stress-life. *Stat Anal Fatigue Data* 91:129–129-9
  25. British Standard (2012) Metallic materials. Fatigue testing. Statistical planning and analysis of data (ISO 12107:2012). BSOL British Standards Online. <https://bsol.bsigroup.com>
  26. Ermakova A, Mehmanparast A, Ganguly S, Razavi J, Berto F (2020) Investigation of mechanical and fracture properties of wire and arc additively manufactured low carbon steel components. *Theor Appl Fract Mech* 109:102685
  27. Ermakova A, Ganguly S, Razavi J, Berto F, Mehmanparast A (2021) Experimental investigation of the fatigue crack growth behavior in wire arc additively manufactured ER100S-1 steel specimens. *Fatigue Fract Eng Mater Struct*. <https://doi.org/10.1111/FFE.13598>
  28. Det Norske Veritas (DNV) (2005) Fatigue design of offshore steel structures. *Recomm Pract DNV-RPC203* 126
  29. Berto F, Campagnolo A, Lazzarin P (2015) Fatigue strength of severely notched specimens made of Ti-6Al-4V under multiaxial loading. *Fatigue Fract Eng Mater Struct* 38:503–517
  30. Razavi SMJ, Van Hooreweder B, Berto F (2020) Effect of build thickness and geometry on quasi-static and fatigue behavior of Ti-6Al-4V produced by Electron Beam Melting. *Addit Manuf* 36:101426
  31. Li P, Warner DH, Fatemi A, Phan N (2016) Critical assessment of the fatigue performance of additively manufactured Ti-6Al-4V and perspective for future research. *Int J Fatigue* 85:130–143
  32. Mehmanparast A, Taylor J, Brennan F, Tavares I (2018) Experimental investigation of mechanical and fracture properties of offshore wind monopile weldments: SLIC interlaboratory test results. *Fatigue Fract Eng Mater Struct* 41:2485–2501
  33. Mehmanparast A, Brennan F, Tavares I (2017) Fatigue crack growth rates for offshore wind monopile weldments in air and seawater: SLIC inter-laboratory test results. *Mater Des* 114:494–504
  34. Anandavijayan S, Mehmanparast A, Braithwaite J, Brennan F, Chahardehi A (2021) Material pre-straining effects on fatigue behaviour of S355 structural steel. *J Constr Steel Res* 183:106707
  35. Corigliano P, Cucinotta F, Guglielmino E, Risitano G, Santonocito D (2020) Fatigue assessment of a marine structural steel and comparison with Thermographic Method and Static Thermographic Method. *Fatigue Fract Eng Mater Struct* 43:734–743
  36. Dantas R, Correia J, Lesiuk G, Rozumek D, Zhu SP, de Jesus A, Susmel L, Berto F (2021) Evaluation of multiaxial high-cycle fatigue criteria under proportional loading for S355 steel. *Eng Fail Anal* 120:105037
  37. Aeran A, Acosta R, Siriwardane SC, Starke P, Mikkelsen O, Langen I, Walther F (2020) A nonlinear fatigue damage model: comparison with experimental damage evolution of S355 (SAE 1020) structural steel and application to offshore jacket structures. *Int J Fatigue* 135:105568
  38. Berto F, Mutignani F, Pittarello L (2016) Effect of hot-dip galvanization on the fatigue behaviour of welded structural steel. *Proc Struct Integr* 2:1813–1820
  39. Atzori B, Berto F, Lazzarin P, Quaresimin M (2006) Multi-axial fatigue behaviour of a severely notched carbon steel. *Int J Fatigue* 28:485–493
  40. Berto F, Lazzarin P, Yates JR (2011) Multiaxial fatigue of V-notched steel specimens: a non-conventional application of the local energy method. *Fatigue Fract Eng Mater Struct* 34:921–943
  41. Berto F, Lazzarin P, Marangon C (2014) Fatigue strength of notched specimens made of 40CrMoV13.9 under multiaxial loading. *Mater Des* 54:57–66

**Publisher's Note** Springer Nature remains neutral with regard to jurisdictional claims in published maps and institutional affiliations.